Power Electronic Systems
Laboratory

Proceedings of the 30th Applied Power Electronics Conference and Exposition (APEC 2015), Charlotte, NC, USA, March 15-19, 2015

10kV SiC-Based Isolated DC-DC Converter for Medium Voltage-Connected Solid-State Transformers

D. Rothmund,
G. Ortiz,
T. Guillod,
J. W. Kolar

Eidgenössische Technische Hochschule Zürich
Swiss Federal Institute of Technology Zurich

10kV SiC-Based Isolated DC-DC Converter for Medium Voltage-Connected Solid-State Transformers

D. Rothmund, G. Ortiz, Th. Guillod, and J. W. Kolar
Power Electronic Systems Laboratory, ETH Zurich
Email: rothmund@lem.ee.ethz.ch

***Abstract*—Silicon-carbide semiconductor technology offers the possibility to synthesize power devices with unprecedented blocking voltage capabilities while achieving outstanding switching and conduction performances. Accordingly, this new semiconductor technology is especially interesting for Solid-State Transformer concepts and is utilized in this paper for designing a 25 kW/50 kHz prototype based on 10 kV SiC devices, featuring a 400 V DC output. The focus is on the DC-DC converter stage while special attention is placed on the large step-down medium frequency transformer, whereby the impact of the rather high operating frequency and high number of turns with respect to the transformer's resonance frequency is analyzed This leads to useful scaling laws for the resonance frequency of transformers in dependence of the operating frequency and construction parameters. Finally, a transformer prototype and efficiency and power density values for the DC-DC stage are presented.**

I. Introduction

Solid-State Transformer (SST) technology enables the incorporation of several novel features to the electric power network, easing, for example, the implementation of the envisioned future Smart Grid [1, 2]. Among the main challenges in the construction of SSTs, the strategies to connect to the Medium-Voltage (MV) level can be highlighted [3, 4]. This problem has been mainly tackled by synthesizing multi-cellular SST concepts based on modules rated for a fractional portion of the total MV side voltage and performing a series connection of these modules at the input side [2, 5].

The development of Silicon-Carbide (SiC) semiconductors opens the possibility to fabricate power semiconductor devices with high blocking voltage capabilities while achieving superior switching and conduction performances. These higher voltage semiconductors enable the construction of single-cell SSTs avoiding the series connection of several modules resulting in simple and reliable converter structures known from lower voltage converters.

On the other hand, in several applications, the migration from traditional AC power distribution to DC supply systems is considered for future installations. Examples are telecommunications [6], information processing facilities [7], and microgrids [8], among others. Previous research has shown that DC bus voltages around 400 V exhibit a favorable trade-off with respect to costs and efficiency of the installation [7]. For this reason, the SST concept designed in this paper is aimed to supply a 400 V DC bus.

One possible implementation of SST technology in DC-supplied facilities is shown in Fig. 1. Here, the MV grid is directly interfaced by respective single-phase SSTs connected in star configuration. These SSTs supply the 400 V loads while providing the required isolation. In addition, battery banks for uninterrupted power supply and/or clean renewable energy sources such as PV arrays can be integrated into the facility. The block diagram of the SST shown in Fig. 1 is shown in Fig. 2 and consists of the input rectifier with its respective EMI filter feeding an isolated DC-DC converter through a 8 kV DC-link. This DC-DC converter realizes the conversion to the desired 400 V at the output of the SST. It should be noted that the rectifier and its respective EMI filter must be analyzed comprehensively, whereby the effects of fast switching transients of SiC semiconductors, which lead to considerably high dv/dt's, are taken into account when selecting the appropriate topology and its switching frequency. For this reason, the main focus is placed on the DC-DC converter whereas the rectifier stage will remain part of future analysis.

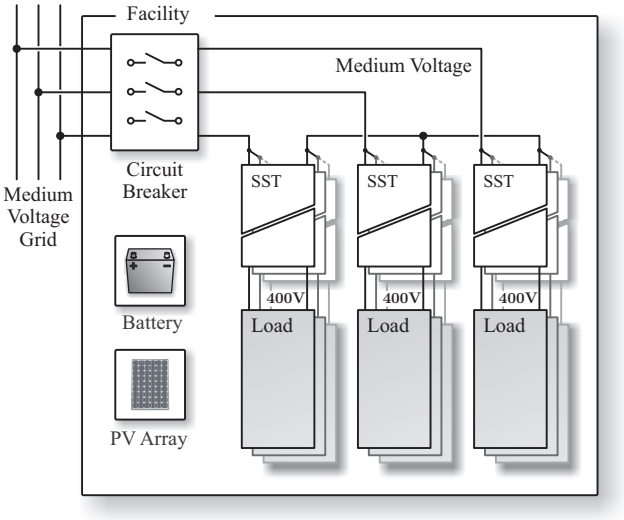

Figure 1: MV-fed facility incorporating 400 V DC bus supplied by SST technology.

Due to the non-modular construction, the Medium-Frequency (MF) transformer must be built with a considerably higher turns ratio, in contrast to MF transformers in multi-cellular SSTs [9–12]. The combination of high turns ratios and larger dimensions due to the higher nominal power can lead to large parasitic components in the MF transformer, decreasing its natural resonance frequency. Given the desire to operate these DC-DC converters at higher frequencies, it results critical to analyze the impact of higher switching frequencies and large turns ratios on the transformer's resonance frequency. For this reason, a dedicated section of this paper focuses on the analysis of the scaling laws linking the operating frequency and turns ratio of the MF transformer to this resonance frequency, where guidelines to build MF transformers with these characteristics will be laid out.

The paper is organized as follows. First, in **Section II** the circuit diagram of power electronic bridges on the MV and LV sides will be presented together with their principles of operation and the resulting power losses and volume of critical components. The MF transformer and the aforementioned scaling laws are presented in **Section III** together with the corresponding experimental verification of the presented transformer scaling laws. **Section IV** summarizes the results and gives the final values for efficiency and power density of the DC-DC stage.

II. Isolated DC-DC Converter Design

For the topology of the isolated DC-DC converter stage, a phase-shift modulated Dual Active Bridge (DAB) (cf. Fig. 3-a)) has been selected, mainly for the reason of clamped switch voltages and the possibility to achieve Zero Voltage Switching (ZVS) for all

978-1-4799-6735-3/15/$31.00 ©2015 IEEE

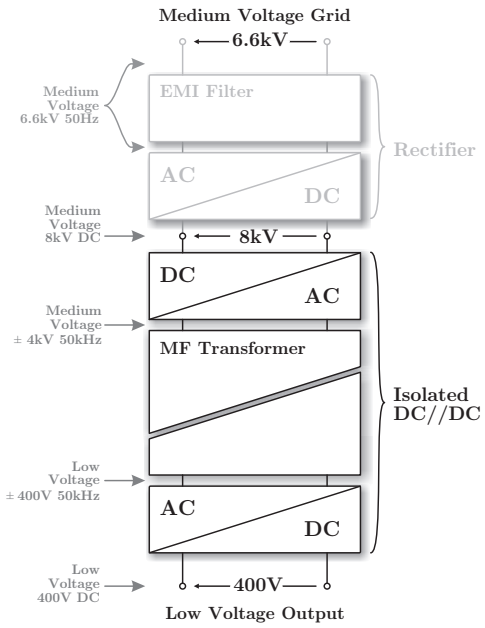

Figure 2: Structure of the SST highlighting the isolated connection between a 8 kV DC-link to a 400 V DC bus through a single-stage (non-series connected) 10kV SiC-based DC-DC converter.

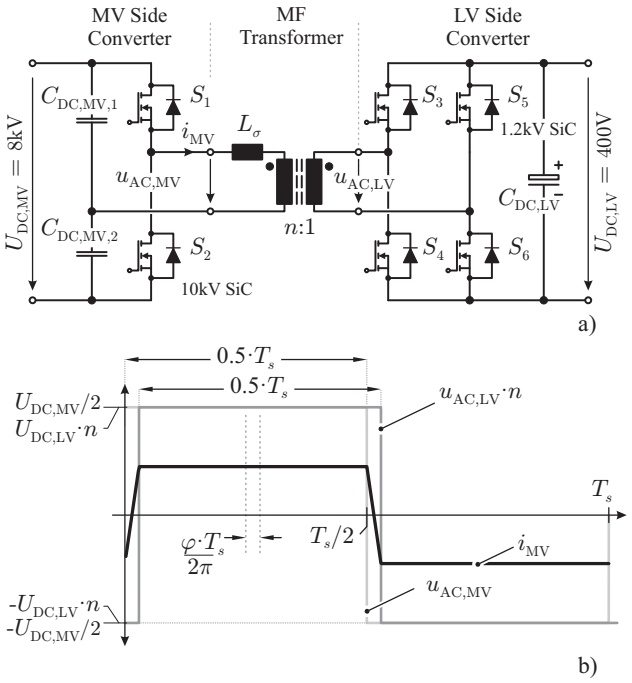

Figure 3: DC-DC converter structure: a) Circuit diagram comprising 10kV SiC devices on the MV side linked through a MF transformer to a 1.2kV SiC-based LV side; b) DC-DC converter waveforms for operation in pure phase-shift mode ($L_\sigma = 352\,\mu\text{H}$, $n = 10$ and $\varphi = 14.4\,^\circ$)

TABLE I: Specifications and characteristics of isolated DC-DC converter.

Parameter	Symbol	Value
Nominal power	P_N	25 kW
Switching frequency	f_s	50 kHz
MV side DC-link voltage	$U_{\text{DC,MV}}$	8 kV
LV side DC-link voltage	$U_{\text{DC,LV}}$	400 V
MV side DC-link capacitance	$C_{\text{DC,MV,1,2}}$	1.25 µF
LV side DC-link capacitance	$C_{\text{DC,LV}}$	50 µF
Transformer leakage inductance	L_σ	352 µH
Transformer turns ratio	n	10 : 1
Nominal phase shift	φ	14.4°
MV side DC-link RMS-current	$I_{\text{rms,C,MV}}$	3.4 A
LV side DC-link RMS-current	$I_{\text{rms,C,LV}}$	20.5 A
MV side switch RMS current	$I_{\text{MV,RMS}}$	4.7 A
LV side switch RMS current	$I_{\text{LV,RMS}}$	46 A
MV side switch resistance	$R_{\text{DS,on,MV}}$	520 mΩ
LV side switch resistance	$R_{\text{DS,on,LV}}$	11.33 mΩ
Cooling System Performance Index	CSPI	10 W/K/dm^3
Total heat sink volume	V_HS	0.36 dm^3

semiconductors in order to allow for a high switching frequency and efficiency. Table I shows the specifications of the DC-DC converter.

This particular topology (cf. Fig. 3) consists of a split DC-link where each capacitor is realized with a series connection of five 1300 V, 5 µF foil capacitors, a half-bridge consisting of 10 kV SiC MOSFETs, a 10 : 1 MF transformer and a SiC MOSFET full-bridge on the LV side. The half bridge configuration is selected due to its rather simple construction and given that the 10 kV SiC devices are properly rated for the resulting higher currents. The required series inductance is directly integrated into the transformer in terms of its leakage inductance. The LV side full-bridge consists of three paralleled 1200 V C2M0025120D MOSFETs per switch in order to reduce the conduction losses. Although the LV side DC-link voltage is only 400 V, these 1200 V SiC devices have been selected due to their outstanding switching behaviour and their low on-state resistance.

The ideal current and voltage waveforms of the considered topology for pure phase-shift modulation with a phase angle φ are shown in Fig. 3-b). As the transformer's turns ratio matches the ratio between the voltages applied from the MV side and LV side power electronic bridges, the current shows an almost rectangular shape, featuring a low RMS value. Furthermore, it can be seen that all semiconductors switch under zero voltage in this operation mode. ZVS transitions are considered with zero losses in the calculations. With these current waveform, the conduction losses of all semiconductors can be calculated based on the given values for on-state resistance $R_{\text{DS,ON}}$.

The DC-link capacitances have been chosen such that the voltage ripple in each capacitor stays below 1 % and such that the specific capacitor is able to handle the current ripple. For the dimensioning of the heat sink, a Cooling System Performance Index [13] of CSPI = 10 has been considered.

With the power electronic components selected, the next step is to analyze the high step-down transformer with special focus on its resonance frequency.

III. Medium-Frequency Transformer

This section analyzes the impact of a higher voltage winding in combination with high operating frequency on the parasitic components, namely the leakage inductance L_σ and the parasitic winding capacitance C_p of the MF transformer. First, a theoretical basis for the analysis of the transformer's resonance frequency will be laid out and later the corresponding experimental verification is presented.

A. MF Transformer Resonance Frequency

The selected transformer geometry is shown in Fig. 4-a) and it exhibits a rotational symmetry in order simplify the analytical calculations as well as the required numerical simulations (even if the results also extend to other geometries). The analysis is however also valid for an E-shaped core. It is also assumed that the isolation

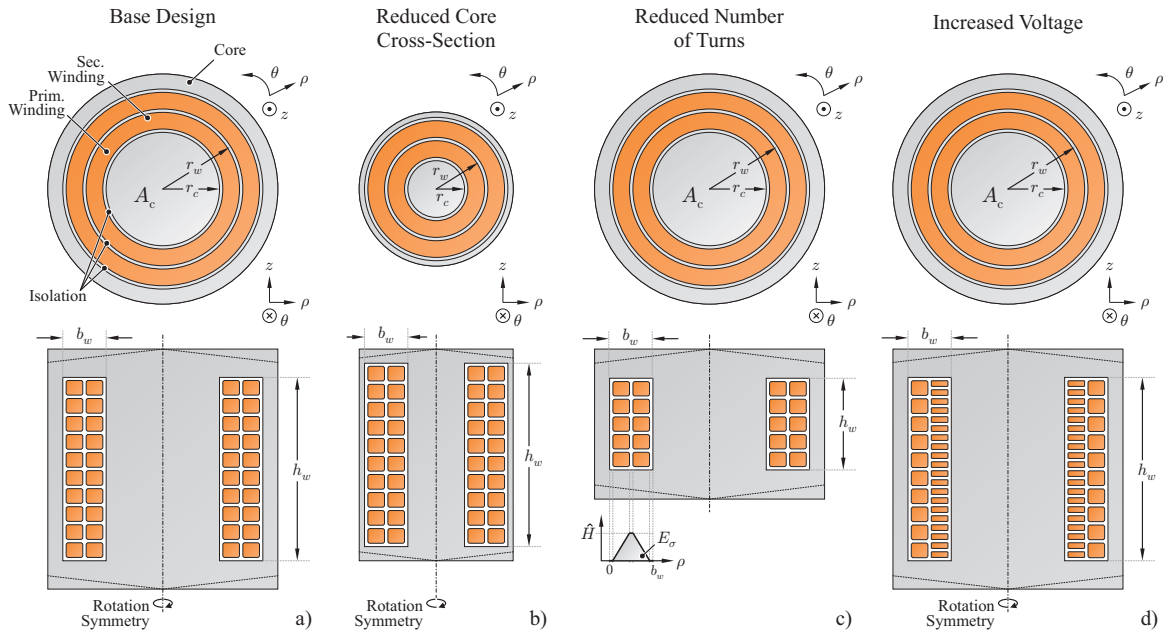

Figure 4: Scaling of the MF transformer for changes in operating frequency and voltage (drawings are not to scale): a) Base design; b) Adaptation of the core cross section A_c to account for operating frequency f_s increase; c) Modification of a) in the number of turns N_1 to account for operating frequency f_s increase; d) Increase of number of turns N_1 to enable operation with higher voltages.

distances are defined from the system's perspective [14] and are therefore not affected by a higher voltage of the primary winding.

For the voltage waveform shown in Fig. 3 and the geometric definitions from Fig. 4-a), the relation between the transformer's primary voltage and the peak flux density is given by:

$$\hat{U}_1 = N_1 A_\mathrm{c} \cdot \frac{\Delta B}{\Delta T} = 4 N_1 A_\mathrm{c} \hat{B} f_\mathrm{s}, \tag{1}$$

where $\hat{U}_1 = U_{\mathrm{DC,MV}}/2$ is the peak primary voltage, N_1 is the number of turns in the primary side of the transformer, A_c is the transformer's core cross section and $f_\mathrm{s} = 1/T_\mathrm{s}$ is the converter's switching frequency. Solving (1) for $N_1 A_\mathrm{c}$ yields

$$N_1 A_\mathrm{c} = \frac{\hat{U}_1}{4 \hat{B} f_\mathrm{s}}. \tag{2}$$

Neglecting thermal considerations [9], for a constant peak flux density $\hat{B}$ and constant peak voltage $\hat{U}_1$, the modification of the transformer's operating frequency must be counteracted by an increase in the transformer's core cross section A_c and/or on the number of turns N_1 on the primary winding (without modifying the turns ratio). For the purpose of analyzing the scaling of the transformer's resonance frequency f_r with respect to the designed operating frequency f_s, these two cases are treated independently. This way, for the scaling of the transformer geometry two cases are identified: 1) constant number of turns

$$A_\mathrm{c} = \frac{\hat{U}_1}{4 \hat{B} N_1 f_\mathrm{s}} = k_\mathrm{A} \frac{1}{f_\mathrm{s}}, \quad k_\mathrm{A} = \frac{\hat{U}_1}{4 \hat{B} N_1} \tag{3}$$

and 2) constant core cross section

$$N_1 = \frac{\hat{U}_1}{4 \hat{B} A_\mathrm{c} f_\mathrm{s}} = k_\mathrm{N} \frac{1}{f_\mathrm{s}}, \quad k_\mathrm{N} = \frac{\hat{U}_1}{4 \hat{B} A_\mathrm{c}}. \tag{4}$$

1) Constant Number of Turns N_1: In this case, the change in operating frequency f_s is counteracted exclusively by modifying the transformer's core cross section A_c in order to maintain equal peak flux density $\hat{B}$. Following the definitions from Fig. 4-b), the radius r_c of the core cross section and the radius of the winding window r_w are expressed as

$$r_\mathrm{c} = \sqrt{\frac{k_\mathrm{A}}{\pi} \cdot \frac{1}{f_\mathrm{s}}} \tag{5}$$

$$r_\mathrm{w} = r_\mathrm{c} + \frac{b_\mathrm{w}}{2} = \sqrt{\frac{k_\mathrm{A}}{\pi} \cdot \frac{1}{f_\mathrm{s}}} + \frac{b_\mathrm{w}}{2}, \tag{6}$$

where b_w is the width of the transformer's winding window.

On the other hand, the leakage inductance L_σ and the equivalent parasitic capacitance C_p of the transformer are determined by

$$L_\sigma = 2\pi r_\mathrm{w} \cdot L'_\sigma \tag{7}$$

$$C_\mathrm{p} = 2\pi r_\mathrm{w} \cdot C'_\mathrm{p}, \tag{8}$$

whereby r_w is the radius of the winding window (cf. Fig. 4-b)), L'_σ and C'_p are the per/unit length leakage inductance and per/unit length parasitic capacitance respectively. From (7) and (8) the expression for the transformer's short circuit resonance frequency f_r is found:

$$f_\mathrm{r} = \frac{1}{r_\mathrm{w} (2\pi)^2 \sqrt{L'_\sigma C'_\mathrm{p}}}. \tag{9}$$

It should be noted that (9) represents the first encountered resonance frequency, whereby other resonances may be found at higher frequencies, as will be shown experimentally in Section III-B. In addition, this resonance is equivalent to that of a parallel resonant circuit with inductance L_σ and capacitor C_p. By combining (6) and (9), the relation for the resonance frequency f_r and the operating frequency of the transformer f_s is found

$$f_\mathrm{r} = \frac{1}{(2\pi)^2 \left(\sqrt{\frac{k_\mathrm{A}}{\pi} \frac{1}{f_\mathrm{s}}} + \frac{b_\mathrm{w}}{2} \right) \sqrt{L'_\sigma C'_\mathrm{p}}}. \tag{10}$$

The expression in (10) shows the dependency of the transformer's natural resonance frequency f_r with respect to the design operating frequency f_s. In order to simplify the analysis, it is assumed that the term $\frac{b_\mathrm{w}}{2}$ is considerably smaller than r_c, thus the resonance frequency f_r can be rewritten as

$$f_\mathrm{r} \approx \frac{1}{(2\pi)^2 \left(\sqrt{\frac{k_\mathrm{A}}{\pi}\frac{1}{f_\mathrm{s}}}\right)\sqrt{L'_\sigma C'_\mathrm{p}}} = \frac{1}{4\pi\sqrt{\pi k_\mathrm{A}\cdot L'_\sigma C'_\mathrm{p}}}\cdot\sqrt{f_\mathrm{s}}. \tag{11}$$

Replacing the value of k_A from (3) results in

$$f_\mathrm{r} \approx \frac{1}{2\pi}\sqrt{\frac{\hat{B}N_1}{\pi\hat{U}_1}}\cdot\frac{1}{\sqrt{L'_\sigma C'_\mathrm{p}}}\cdot\sqrt{f_\mathrm{s}} = k_1\cdot\sqrt{f_\mathrm{s}}. \tag{12}$$

From (12), it can be seen that for the case when the modification of switching frequency is accounted by exclusively modifying the core cross section A_c, the relation between the operating frequency f_s and the resonance frequency f_r follows a square root function. As a result, (12) shows that if the operating frequency f_s is increased linearly, the resonance frequency f_r increases at a slower rate, meaning that at higher operating frequencies they will come in close vicinity, leading to undesired resonances in the transformer windings [15].

2) Constant Core Cross Section A_c: Next, the analogous case of transformer resonance frequency scaling will be shown for constant core cross section A_c and adjusting the winding window geometry in order to accommodate the number of turns N_1 accordingly and finally to adapt the transformer geometry to the new operating frequency f_s. This geometry modification impacts the leakage inductance L_σ as well as the parasitic capacitance C_p value, as will be analyzed in the following.

Consider the winding window arrangement as shown in Fig. 4-c). From here, the total stored leakage energy E_σ can be found [16]:

$$E_\sigma = \frac{\mu_0}{2}\int_V H(x,y,z)^2 dV, \tag{13}$$

where μ_0 is the permeability of air. For the geometric definitions in Fig. 4-c), (13) can be approximately simplified to

$$E_\sigma = \frac{\mu_0}{2}2\pi r_\mathrm{w} h_\mathrm{w}\int_{r_\mathrm{c}}^{r_\mathrm{c}+b_\mathrm{w}} H(\rho)^2 d\rho \tag{14}$$

$$= \frac{\mu_0}{2}2\pi r_\mathrm{w} h_\mathrm{w}\cdot\hat{H}^2\int_{r_\mathrm{c}}^{r_\mathrm{c}+b_\mathrm{w}} h(\rho)^2 d\rho, \tag{15}$$

where $h(\rho)$ is the normalized H field value which is not depending on frequency but only depends on the geometry of the winding window in the ρ direction (cf. Fig. 4-c)). The peak value of the H field $\hat{H}$ in the winding window is found as

$$\hat{H} = \frac{N_1\hat{I}_1}{h_\mathrm{w}}. \tag{16}$$

Replacing (16) in (15) results in

$$E_\sigma = \hat{I}_1^2 N_1\left(\frac{N_1}{h_\mathrm{w}}\right)\pi r_\mathrm{w}\mu_0\cdot D, \tag{17}$$

where $\hat{I}_1$ is the peak current in the primary winding and D represents the solution for the integral at the right hand side of (15). Equating (17) to the equivalent leakage inductance energy and solving for the leakage inductance L_σ gives

$$L_\sigma = N_1\left(\frac{N_1}{h_\mathrm{w}}\right)2\pi r_\mathrm{w}\mu_0 D. \tag{18}$$

Assuming an increase in the primary turns N_1 leads to a proportional increase in h_w, then the term (N_1/h_w) in (18) is assumed constant. This way, the expression in (4) is replaced in (18), giving

$$L_\sigma = \frac{\hat{U}_1}{2A_\mathrm{c}\hat{B}}\left(\frac{N_1}{h_\mathrm{w}}\right)\pi r_\mathrm{w}\mu_0 D\cdot\frac{1}{f_\mathrm{s}}. \tag{19}$$

From (19) it can be seen that an inversely proportional relation exists between the leakage inductance L_σ and the operating frequency f_s when a modification of this operating frequency is counteracted by modifying the number of turns N_1.

Similar as for the previous case (constant number of turns N_1), for the parasitic capacitance C_p a linear relation between the number of primary turns N_1 and the parasitic capacitance C_p is considered:

$$C_\mathrm{p} = C''_\mathrm{p}\cdot N_1, \tag{20}$$

where C''_p is the capacitance per/unit length in the θ direction of the winding window. Replacing (4) in (20) results in:

$$C_\mathrm{p} = \frac{\hat{U}}{4A_\mathrm{c}\hat{B}}C''_\mathrm{p}\cdot\frac{1}{f_\mathrm{s}}. \tag{21}$$

Combining (19) and (21), the product $L_\sigma C_\mathrm{p}$ is found as

$$L_\sigma C_\mathrm{p} = \frac{1}{8}\left(\frac{\hat{U}}{A_\mathrm{c}\hat{B}}\right)^2\cdot\frac{N_1}{h_\mathrm{w}}C''_\mathrm{p}\pi r_\mathrm{w}\mu_0 D\cdot\frac{1}{f_\mathrm{s}^2}. \tag{22}$$

Finally, the expression for the resonance frequency f_r depending on operating frequency f_s for scaling of the number of turns N_1 is found

$$f_\mathrm{r} = \frac{A_\mathrm{c}\hat{B}}{\hat{U}\pi\sqrt{\frac{1}{2}C''_\mathrm{p}\pi r_\mathrm{w}\mu_0 D\frac{N_1}{h_\mathrm{w}}}}\cdot f_\mathrm{s}. \tag{23}$$

The expression in (23) shows that there exists a linear relation between the resonance frequency f_r and the operating frequency f_s when the modification in f_s is counteracted by exclusively modifying the number of turns N_1 of the transformer.

This and the first case of transformer's resonance frequency scaling will be validated through numerical simulations in the following.

3) Validation Through FEM Analysis: Simulations have been performed in order to verify the aforementioned scaling laws. The analytical expressions will be studied at different points in order to prove the predictability of the model.

Since, per definition, the resonance of a transformer involves the electric and the magnetic fields, a fully coupled simulation has to be performed. 3D fully coupled simulations require considerably high computing power and the accurate modeling of the high frequency losses is relatively complex. For this reason, a hybrid 2D/3D method has been conducted. This numerical method can be split into three steps as shown in Fig. 5:

- First the inductance and capacitance matrix are extracted in 2D. Every turn and every winding is modeled and the coupling between all these wires is extracted. A commercial FEM solver has been used.
- The Partial Element Equivalent Circuit method (PEEC) is used to build a 3D equivalent circuit of the transformer [17, 18]. The inductance and capacitance from the 2D FEM simulation are used, completed with direct 3D analytical computation. This step is performed with a custom made solver.

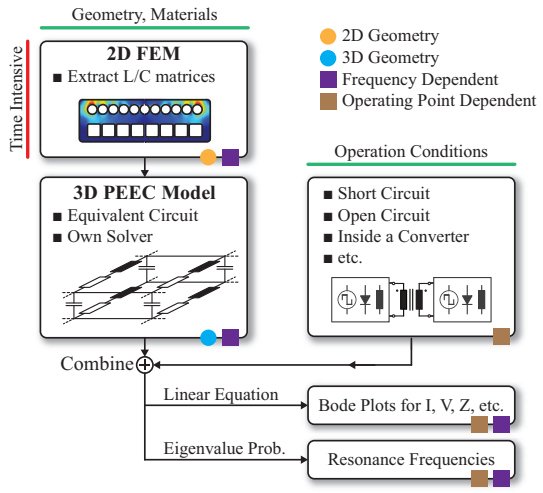

Figure 5: Methodology for extraction of transformer's resonance frequency utilizing FEM and PEEC modelling.

- The equivalent circuit is connected for measuring the short circuit impedance from the primary side. Afterwards, the current and voltage can be extracted for different frequencies and the resonance can be found. If only the resonance is of interest (and not the complete impedance plot), a generalized eigenvalue problem can be posed, which provides directly all resonances of the system [19].

This method includes the following phenomena: skin and proximity effects, magnetic losses and frequency dependence of the core properties. The high frequency effects are particularly important for resonance computation since the resonances are occurring at frequencies where the losses are significant. The computation time is several orders of magnitude smaller than the fully coupled 3D FEM simulations.

A series of simulations utilizing the aforementioned method were conducted for the analyzed scaling laws for both constant number of turns (cf. Section III-A1) and constant core cross section (cf. Section III-A2). The simulated results for the resonance frequency, normalized with respect to the base design, are shown in Fig. 6, where the operating frequency has also been normalized with respect to the base design. The base design consists of a $N_1/N_2 = 9:9$ transformer with three layers on the primary winding and a single layer on the secondary winding.

As can be seen in Fig. 6, the previous analysis for the resonance frequency in dependence of the operating frequency shows the predicted behavior for the constant core cross section A_c case, where the simulated values follow closely the ones obtained with (23).

For the case with constant number of turns N_1, the approximated values calculated from (12) differ from the simulated values at higher frequencies, given that the assumption $b_w/2 << r_c$ is no longer valid. If this approximation is discarded, i.e. (10) is directly utilized, the calculated scaling of resonance frequency follows closely the simulated results, as shown in Fig. 6 for the constant N_1 case without approximation.

The FEM simulation tools prove useful for the validation of the theoretically formulated expressions, whereby, in order to increase the resonance frequency of the transformer, a scaling of the number of turns should be preferred as opposed to a scaling of the core cross section when a higher operating frequency is desired.

The introduced FEM simulation tool is now used to study the impact of a high number of turns N_1, i.e. a high turns ratio n (resulting from a required high voltage winding) on the transformer's

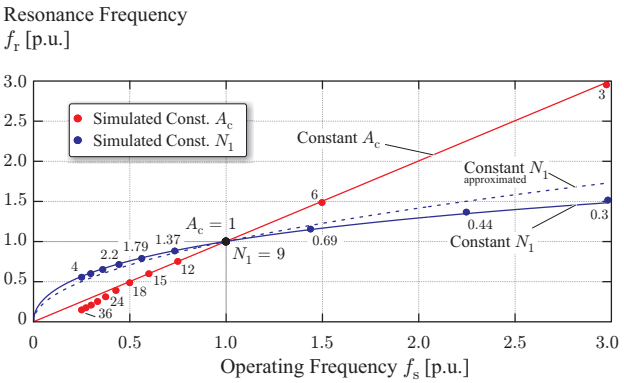

Figure 6: Dependency of transformer's resonance frequency for modification in the operating frequency. Two cases are considered for the scaling of the transformer: constant number of turns (cf. Section III-A1) and constant core cross section (cf. Section III-A2). The core cross-section A_c is normalized with respect to the base value.

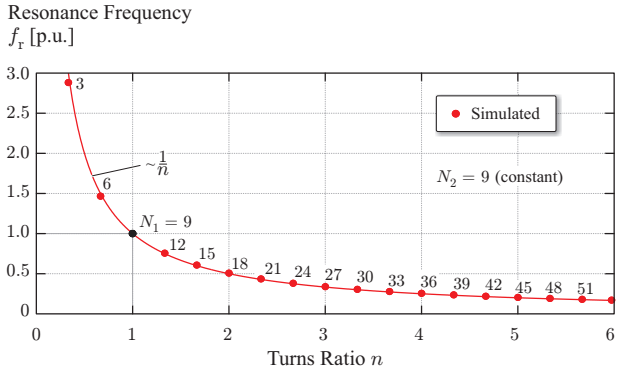

Figure 7: Effect of increased number of turns on transformer's resonance frequency f_r for a constant operating frequency f_s.

resonance frequency f_r.

4) Effect of High Turns Ratio: It results interesting to analyze the proportionality factor relating the resonance frequency f_r and the operating frequency f_s in order to find the impact of constructing a transformer with a higher peak primary voltage $\hat{U}_1$, i.e. a higher number of turns N_1. It should be noted that, since the transformer power is kept unchanged, the cross section of the copper conductor should be reduced proportionally in order to keep the current density constant, as shown in Fig. 4-d). This way, only a larger number of primary side turns N_1 is accommodated in the winding window, thus the formulae from Section III-A1 is utilized in this case given that the winding window geometry is unchanged (cf. Figs 4-a) and d)).

From (12), the proportionality factor linking the resonance frequency f_r to the operating frequency f_s is found as

$$k_1 = \frac{1}{2\pi}\sqrt{\frac{\hat{B}N_1}{\pi\hat{U}_1}} \cdot \frac{1}{\sqrt{L'_\sigma C'_p}}. \tag{24}$$

Assuming a constant peak flux density $\hat{B}$, the left hand side term of (24) is constant given that an increase in peak voltage $\hat{U}_1$ would lead to a proportional increase in the number of turns N_1 in order to keep the peak flux density $\hat{B}$ constant. An increase in N_1, however, would affect the term $L'_\sigma C'_p$ on the right hand side of (24). Given it's rather complex analytical modeling, the link between the constant k_1 and the value of the parasitic components L'_σ and C'_p was studied utilizing the previously introduced FEM simulation tools.

TABLE II: Constructed transformers' (cf. Fig. 8) geometrical values. The peak flux density is in all cases $\hat{B} = 0.2\,\mathrm{T}$.

f_s [kHz]	N_1/N_2	h_w [mm]	b_w [mm]	r_c [mm]	r_w [mm]
25				47.5	57.5
50	70/7	53	24	27.5	39.5
83				22.5	33.8

TABLE III: Measured (cf. Fig. 9) and theoretical values for resonance frequency scaling with constant number of turns N_1.

Op. Freq.	Calc. Res Freq.	Meas. Res Freq.	Error	$f_\mathrm{r}/f_\mathrm{s}$
25 kHz	Base Value	387 kHz	-	15.5
50 kHz	563 kHz	537 kHz	5.0 %	10.7
83 kHz	659 kHz	640 kHz	3.1 %	7.7

The results for this analysis are shown in Fig. 7. Here a clear dependency of the transformer's resonance frequency f_r with respect to the turns ratio, and consequently on the number of turns N_1 on the primary winding, can be seen, as for higher number of turns N_1, the resonance frequency with respect to the base design is considerably reduced, imposing a limitation on the achievable turns ratio n of the transformer.

In addition, it can be seen that, for the simulated case, the decrease in resonance frequency f_r with respect to the turns ratio n follows a $1/n$ behavior, as shown in Fig. 7. This relation, however, is strongly dependent on the winding strategy (e.g. number of layers, required isolation, etc.) and thus an analytical expression which considers all these aspects should be elaborated.

Fig. 7 highlights the limitation found when constructing transformers for higher voltages and higher frequencies, as the operating frequency f_s comes in close vicinity to the resonance frequency f_r, which could result in an unsuitable transformer design.

B. Experimental Verification

To prove the previously described theoretical and simulated analysis, three transformers for different frequencies were constructed and are presented in Fig. 8. The design parameters of these transformers are shown in Table II. The three selected operating frequencies are $f\mathrm{s} = 25\,\mathrm{kHz}$, $f\mathrm{s} = 50\,\mathrm{kHz}$ and $f\mathrm{s} = 83\,\mathrm{kHz}$, all for a nominal power of P_N=25 kW. In order to emulate the rotational symmetric arrangements presented in Fig. 4, these transformers are based on several pairs of UR 64-40-20 U cores (ferrite 3C90 material) arranged as shown in Fig. 8. With this construction, the case of constant number of turns N_1 (adaptation of the core cross section A_c to the operating frequency modification) is experimentally analyzed, which is feasible from a practical point of view in contrast to the scaling of the number of turns which would require a modification of the winding window geometry while keeping a constant core cross section A_c.

The impedances of the transformers presented in Fig. 8 (with short circuited secondary windings) are shown in Fig. 9. Here, the resonance peaks of each design are visible, whereby the resonance frequency values can be extracted for each transformer design.

Utilizing the 25 kHz design as base value and the respective scaling law derived in Section III, the resonance frequencies for the 50 kHz and 83 kHz designs can be calculated, whereby the obtained values are presented in Table III together with the measurements shown in Fig. 9. As can be seen from the calculated relative errors, a good agreement of the measured and calculated values for resonance frequency is obtained, proving the validity of the theoretical and simulated results from the previous sections.

The resulting resonance frequencies for all transformer designs are well above the operating frequency, as shown by the $f_\mathrm{r}/f_\mathrm{s}$ ratio in Table III. It should be noted, however, that this ratio decreases for higher operating frequencies and is below 10 for the highest frequency design. This fact empirically shows the requirement of careful transformer concept selection when higher frequencies and higher voltages, leading to higher number of turns, are required.

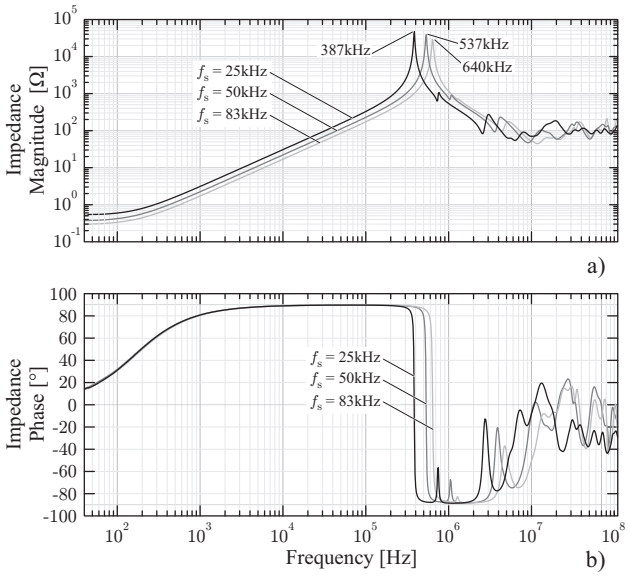

Figure 9: Measured short circuit impedance a) magnitude and b) phase of the three constructed transformers.

To finalize the analysis, the $f_\mathrm{s} = 50\,\mathrm{kHz}$ transformer was excited from the primary winding (with shorted secondary winding) by a SiC-based converter bridge in order to visualize the transformer's response in time domain. The results for a switched current of 2 A and 10 A are shown in Figs. 10-a) and c) respectively. These waveforms show that the transformer behaves purely inductive, given the operation well below the resonance frequency (cf. Fig. 9). Moreover, the detailed view of the transformer current i_MV during switching action for the 2 A case, presented in Fig. 10-b) indicates that the excited resonance frequencies are of higher order ($\sim 10\,\mathrm{MHz}$) and correspond to the peaks beyond the first resonance for the 50 kHz design in Fig. 9. This is due to the voltage source-type behavior of the converter bridge, whereby the first resonance results in a low admittance value seen from the converter bridge and only the aforementioned higher resonances are excited.

To validate the previous analysis, the measured waveform for i_MV in Figs. 10-b) and d) was reconstructed based on the measured voltage excitation and the measured impedance from Fig. 9. This reconstruction is done with the Fourier transform of the voltage multiplied by the measured transformer admittance in the frequency domain. The results are also depicted in Figs. 10-b) and d) where a good agreement of the reconstructed $i_\mathrm{MV,Cal}$ and measured current i_MV waveforms can be seen.

Furthermore, the increase of switched current to 10 A reduces considerably the effect of the aforementioned resonances (cf. Fig. 10-d), due to the reduction of the voltage's dv/dt achieved by the operation of the bridge in soft-switching mode. This fact renders the utilization of soft switching modulation schemes especially important for higher frequency transformers with higher step down ratios. In addition, the good matching of the reconstructed and the measured time waveforms imply that the power electronic bridge has negligible influence on the transformer resonances. Particularly, the large SiC MOSFETS capacitance does not interfere with the transformer resonance.

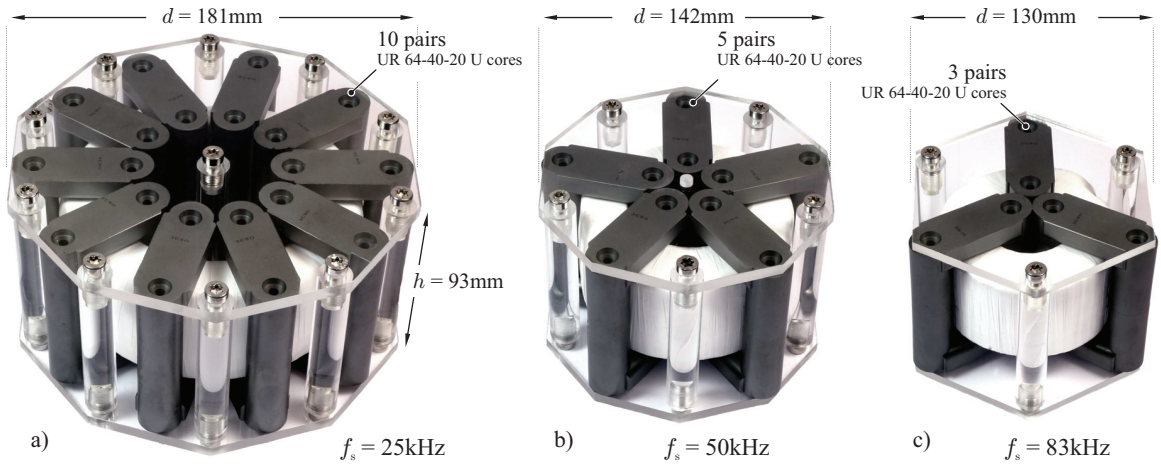

Figure 8: Constructed 25 kW MF transformer prototypes for a) 25 kHz, b) 50 kHz and c) 83 kHz.

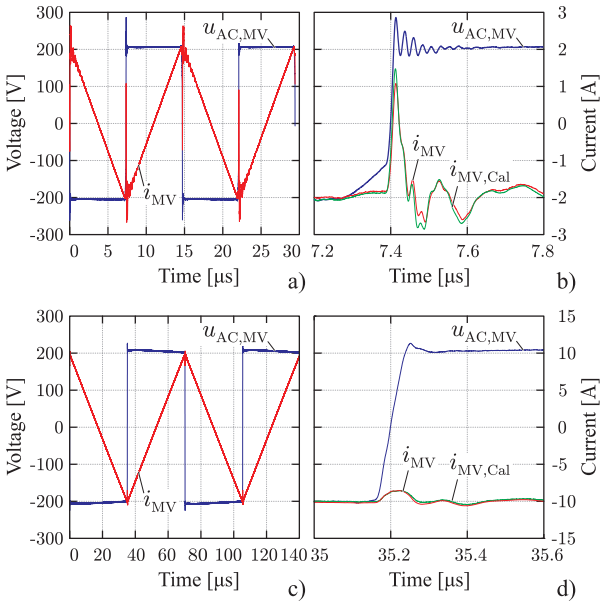

Figure 10: Time domain measurements on the 50 kHz transformer prototype with a)-b) 2 A of switched current and c)-d) with 10 A of switched current.

IV. Summary of Results

In order to summarize the design results, a loss breakdown and a volume breakdown of the DC-DC converter is given in Fig. 11. Although each LV side switch consists of three parallel C2M0025120D MOSFETs, the losses of the LV side switches contribute 46 % to the overall losses whereas the transformer causes 41 % of the total losses. The critical parts, namely the 10 kV SiC-MOSFETs, cause only 11 % of the losses due to the relatively low MV side current and thus low conduction losses. This results in a relatively simple cooling concept for the MV side MOSFETs, in spite the thermal interface between the device's junction and the heat sink has to be designed for an isolation voltage of 10 kV.

The volume breakdown in Fig. 11 shows that the transformer accounts for 70 % of the converter volume (excluding auxiliary circuitry) whereas the heat sink and the DC-link share the rest of the volume approximately equally. The reason for this is that the transformer has to provide the galvanic isolation for at least 10 kV which requires a large part of the space in the winding window for isolation material.

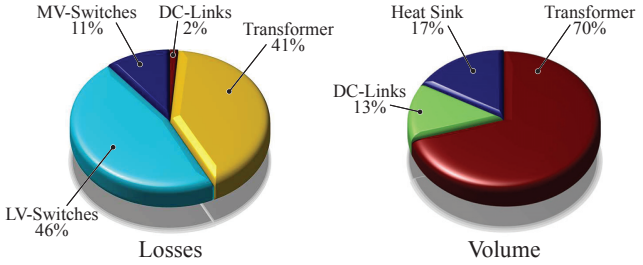

Figure 11: Loss and volume breakdown of the 25 kW/50 kHz, 8 kV to 400 V DC-DC converter stage.

The total losses of the DC-DC converter are 207 W whereas the total volume is 4.3 dm^3 (including a volume utilization factor of 50 % due to high isolation distances). This leads to a total efficiency of 99.17 % and a power density of 5.8 $\mathrm{kW/dm}^3$.

V. Conclusion

A 10 kV SiC-based converter for directly interfacing the MV grid to a 400 V DC net utilizing SST technology has been discussed. The focus is placed on the DC-DC conversion stage since it integrates the MF transformer where a considerably large voltage step down ratio is required. Special attention is placed on the impact of increased operating frequencies of this large step down transformers on their resonance frequency. Theoretical analysis and FEM simulations resulted in two cases for scaling of the transformer's resonance frequency: constant core cross section and constant number of turns. The latter results in a square-root type relation between operating and resonance frequency while the former presents a linear relation between these frequencies, rendering this last option better suited for the construction of higher voltage MF transformers. Moreover, the number of turns of the primary winding possess a strong influence on the resonance frequency, whereby special attention should be placed when designing transformers with higher frequencies and/or higher voltages as the operating and resonance frequencies could come in close vicinity.

Finally, the theoretical and simulated analysis were backed up by corresponding experimental data extracted from three constructed 25 kW transformer prototypes, where a good agreement of the calculated and measured values was achieved. With these experimental measurements, the complete DC-DC converter stage is dimensioned, reaching an efficiency of 99.17 % and a power density of 5.8 $\mathrm{kW/dm}^3$.

References

[1] J. Wang, A. Huang, W. Sung, Y. Liu, and B. Baliga, "Smart Grid Technologies," *IEEE Industrial Electronics Magazine*, vol. 3, no. 2, pp. 16–23, Jun. 2009.

[2] A. Watson, "UNIFLEX: Report on Hardware Evaluation," University of Nottingham, Tech. Rep., 2009.

[3] J. E. Huber and J. W. Kolar, "Optimum Number of Cascaded Cells for High-Power Medium-Voltage Multilevel Converters," in *IEEE Energy Conversion Congress and Exposition (ECCE)*, Denver, Sep. 2013, pp. 359–366.

[4] D. Dujic, A. Mester, T. Chaudhuri, F. Canales, and J. Steinke, "Laboratory Scale Prototype of a Power Electronic Transformer for Traction Applications," in *European Conference on Power Electronics and Applications (EPE)*, vol. i, Birmingham, 2011, pp. 1–10.

[5] J. W. Kolar and G. Ortiz, "Solid-State-Transformers: Key Components of Future Traction and Smart Grid Systems," in *International Power Electronics Conference (IPEC)*, Hiroshima, 2014.

[6] H. Ikebe, "Power Systems for Telecommunications in the IT Age," in *International Telecommunications Energy Conference (INTELEC)*, Yokohama, 2003, pp. 1–8.

[7] A. Pratt, P. Kumar, and T. V. Aldridge, "Evaluation of 400V DC Distribution in Telco and Data Centers to Improve Energy Efficiency," in *International Telecommunications Energy Conference (INTELEC)*, Rome, 2007, pp. 32–39.

[8] T. Dragicevic, J. C. Vasquez, J. M. Guerrero, and D. Skrlec, "Advanced LVDC Electrical Power Architectures and Microgrids: A Step Toward a New Generation of Power Distribution Networks." *IEEE Electrification Magazine*, vol. 2, no. 1, pp. 54–65, Mar. 2014.

[9] G. Ortiz, M. Leibl, J. W. Kolar, and O. Apeldoorn, "Medium Frequency Transformers for Solid-State-Transformer Applications - Design and Experimental Verification," in *International Conference on Power Electronics and Drive Systems (PEDS)*, Apr. 2013, pp. 1285–1290.

[10] I. Villar, L. Mir, I. Etxeberria-Otadui, J. Colmenero, X. Agirre, and T. Nieva, "Optimal Design and Experimental Validation of a Medium-Frequency 400kVA Power Transformer for Railway Traction Applications," in *IEEE Energy Conversion Congress and Exposition (ECCE)*, Raleigh, Sep. 2012, pp. 684–690.

[11] H. Hoffmann and B. Piepenbreier, "Medium Frequency Transformer for Rail Application using New Materials," in *Electric Drives Production Conference (EDPC)*, Nuremberg, 2011, pp. 192–197.

[12] M. Steiner and H. Reinold, "Medium Frequency Topology in Railway Applications," in *European Conference on Power Electronics and Applications (EPE)*, Aalborg, 2007, pp. 1–10.

[13] U. Drofenik, G. Laimer, and J. W. Kolar, "Theoretical Converter Power Density Limits for Forced Convection Cooling," in *Power Conversion and Intelligent Motion (PCIM Europe)*, Nuremberg, 2005, pp. 608–619.

[14] T. Guillod, J. E. Huber, G. Ortiz, A. De, C. M. Franck, and J. W. Kolar, "Characterization of the voltage and electric field stresses in multi-cell solid-state transformers," in *Energy Conversion Congress and Exposition (ECCE)*, Pittsburgh, Sep. 2014, pp. 4726–4734.

[15] A. Tripathi, K. Mainali, D. Patel, and K. Hauta, "Design Considerations of a 15kV SiC IGBT Enabled High-Frequency Isolated DC-DC Converter," in *International Power Electronics Conference (IPEC)*, Hiroshima, 2014, pp. 758–765.

[16] G. Ortiz, J. Biela, and J. W. Kolar, "Optimized Design of Medium Frequency Transformers with High Isolation Requirements," in *Annual Conference of the IEEE Industrial Electronics Society (IECON)*, Glandale, 2010, pp. 631–638.

[17] J. Smajic and T. Steinmetz, "Simulation and Measurement of Lightning-Impulse Voltage Distributions Over Transformer Windings," *IEEE Transactions on Magnetics*, vol. 50, no. 2, pp. 2–5, 2014.

[18] A. E. Ruehli, "Equivalent Circuit Models for Three-Dimensional Multiconductor Systems," *IEEE Transactions on Microwave Theory and Techniques*, vol. 22, no. 3, pp. 216–221, 1974.

[19] W. J. Tzeng and F. Y. Wu, "Theory of Impedance Networks: the Two-Point Impedance and LC Resonances," *Journal of Physics A: Mathematical and General*, vol. 39, no. 27, pp. 8579–8591, Jul. 2006.